

## Dichroism in the Interaction between Vortex Electron Beams, Plasmons, and Molecules

A. Asenjo-García<sup>1</sup> and F. J. García de Abajo<sup>1,2,\*</sup>

<sup>1</sup>ICFO-Institut de Ciències Fotòniques, Mediterranean Technology Park, 08860 Castelldefels (Barcelona), Spain

<sup>2</sup>ICREA-Institució Catalana de Recerca i Estudis Avançats, Passeig Lluís Companys 23, 08010 Barcelona, Spain

(Received 12 December 2013; revised manuscript received 8 March 2014; published 6 August 2014)

We study the transfer of orbital angular momentum between vortex electron beams and chiral samples, such as staircase plasmonic nanostructures and biomolecules. Inelastic electron scattering from these samples produces large dichroism in the momentum-resolved electron energy-loss spectra. We illustrate this phenomenon with calculations for chiral and nonchiral clusters of silver spheres using both focused and extended electron beams, which exhibit  $\sim 10\%$  difference between channels of opposite angular momentum. In addition to its fundamental interest, this remarkably high dichroism suggests a way of spatially resolving chiral optical excitations, including dark plasmons. We also predict a dichroic response when probing a chiral biomolecule, which suggests the use of these electron beams for resolving different enantiomers.

DOI: 10.1103/PhysRevLett.113.066102

PACS numbers: 68.37.Ma, 42.50.Tx, 73.20.Mf, 79.20.Uv

Vortex electron beams, which are known to exist as propagating solutions of the Schrödinger equation in free space [1], have been recently generated by passing electron beams through different types of phase masks [2–5] in order to select specific values of the orbital angular momentum (OAM). Following a previous suggestion [1,6], electron vortices have been additionally generated by exploiting the interaction between an electron beam and an effective magnetic monopole [7]. These advances have stimulated innovative ways of using electron beams to interact with nanostructured materials. For instance, electron vortices possess a magnetic moment proportional to the OAM that can make them excellent probes of core-level magnetic transitions. Recently, many works have analyzed the range of applicability of these vortices for performing magnetic chiral dichroism [8–10]. A similar effect has been proposed for mapping plasmons in nanostructures [11]. Additionally, the interaction with a longitudinal magnetic field has been predicted to produce Faraday rotation on the electron vortex [12]. This configuration has been also proposed as a way to observe the Aharonov-Bohm effect [13]. Chiral electron beams have even been postulated as suitable tools for inducing and controlling mechanical rotation of nanoparticles [14,15].

Electron vortex beams can be equally used to characterize the optical response of chiral (mirror-symmetry-breaking) structures. Traditionally, circularly polarized light, which carries spin angular momentum, has been used to probe chiral samples, as they produce polarization-dependent absorption cross sections (i.e., circular dichroism [16,17]). However, OAM dichroism cannot be observed when probing with optical Laguerre-Gauss beams [18–22], clearly revealing that chiral light-matter coupling is exclusively mediated by the intrinsic angular momentum of light. In contrast, electrons can undergo chiral transfer of OAM [20].

In this Letter, we demonstrate the chiral exchange of OAM between vortex electron beams and two different kinds of chiral samples: plasmonic nanostructures and biomolecules. In particular, we predict large differences in the intensity of opposite OAM components of electrons that are inelastically scattered from chiral clusters formed by closely arranged silver nanospheres, both under broad and focused vortex beam illumination. The latter can be used to map plasmonic chiral modes with high spatial resolution. We also predict significant dichroism in the electron energy-loss signal produced by  $\alpha$ -helix molecules.

*Energy loss probability.*—We intend to study the probability that an electron prepared in incident state  $i$  undergoes inelastic transitions to final states  $f$ , accompanied by a net transfer of OAM and energy to a chiral sample. The transition rate is given by [23]

$$\frac{d\Gamma_{fi}}{dt} = \int d\omega \frac{d\Gamma_{fi}(\omega)}{dt},$$

where

$$\begin{aligned} \frac{d\Gamma_{fi}(\omega)}{dt} = & \frac{2\hbar e^2}{\omega^2 m_e^2} \int d^3\mathbf{r} d^3\mathbf{r}' \psi_f(\mathbf{r}) \psi_f^*(\mathbf{r}') \delta(\varepsilon_f - \varepsilon_i + \omega) \\ & \times [\nabla \psi_i^*(\mathbf{r})] \cdot \text{Im}\{\mathcal{G}(\mathbf{r}, \mathbf{r}', \omega)\} \cdot [\nabla \psi_i(\mathbf{r}')], \end{aligned} \quad (1)$$

is the spectrally resolved rate,  $\hbar\varepsilon_i$  and  $\hbar\varepsilon_f$  are the initial and final electron energies, and  $\mathcal{G}(\mathbf{r}, \mathbf{r}', \omega)$  is the electromagnetic Green tensor, which contains the fully retarded response of the sample (see the Supplemental Material [24]). The wave functions of energetic beam electrons can be well described as [23]

$$\psi_{i,f}(\mathbf{r}) = \frac{1}{\sqrt{L}} e^{ip_{z,i}z} \psi_{i,f\perp}(\mathbf{R}), \quad (2)$$

where we assume a plane wave behavior along the beam direction  $z$ ,  $L$  is the quantization length along that direction, and the dependence on transversal coordinates  $\mathbf{R} = (x, y)$  is separated in  $\psi_{i,f\perp}(\mathbf{R})$ . The low-kinetic energies associated with the latter allows us to approximate the frequency transfer by  $\omega = \varepsilon_i - \varepsilon_f \approx q_z v$  (nonrecoil approximation), where  $q_z = p_{zi} - p_{zf}$  is the wave vector transfer and  $v$  is the electron velocity ( $v = 0.55c$  for the 100 keV electrons considered in this work). Using Eq. (2) in Eq. (1), summing over final longitudinal wave vectors  $p_{zf}$ , and dividing by the electron current  $v/L$  derived from  $\psi_i$ , we find the probability that an electron undergoes a transition between  $\psi_{i\perp}$  and  $\psi_{f\perp}$  transversal states to have the form (see the Supplemental Material [24])

$$\Gamma(\omega) = \frac{4e^2\omega^2}{\pi\hbar v^4\gamma^2} \sum_{f\perp} \text{Im}\{\mathbf{N}^+ \cdot \boldsymbol{\alpha} \cdot \mathbf{N}\},$$

where  $\gamma = 1/\sqrt{1 - (v/c)^2}$ ,  $\boldsymbol{\alpha}$  is a generalized polarizability matrix describing the response of the sample (see below), and  $\mathbf{N}$  is an electromagnetic matrix element.

*Chiral plasmonic cluster.*—Electron beams are valuable tools to spectrally and spatially map nanoscale plasmons, the collective oscillations of conduction electrons in metals [29,30]. Here, we consider plasmons in chiral clusters formed by non-mirror-symmetric geometrical arrangements of metallic spherical nanoparticles [31,32]. Four spheres are the minimum required to produce a chiral cluster [33]. In particular, we focus on a staircase tetramer and its mirror image, along with a nonchiral planar trimer. For simplicity, the particles are assumed to be small enough as to describe them through a scalar electric polarizability  $\alpha(\omega)$ , which turns out to be a good approximation for the 30 nm silver spheres separated by 5 nm gaps that we study below (see Fig. S2 in the Supplemental Material [24]). Simultaneously, the particle size and spacings are large enough to allow us to describe them using local classical theory [34]. We obtain  $\alpha(\omega)$  using a tabulated dielectric function for silver [35]. For such clusters, we have

$$\boldsymbol{\alpha} = \frac{\mathbf{1}}{\alpha^{-1} - \mathcal{G}_0},$$

where  $\mathcal{G}_{jj'}^0$  describes the retarded interaction between particle dipoles at positions  $\mathbf{r}_j$  and  $\mathbf{r}_{j'}$ , and we use matrix notation with indices running over the three Cartesian directions for each and all of the spheres. The electromagnetic matrix element associated with particle  $j$  is then (see the Supplemental Material [24])

$$\begin{aligned} \mathbf{N}_j &= e^{iq_z z_j} \int d^2\mathbf{R} \psi_{f\perp}^*(\mathbf{R}) \psi_{i\perp}(\mathbf{R}) \\ &\times \left[ \frac{\mathbf{u}_j}{|\mathbf{u}_j|} K_1\left(\frac{q_z |\mathbf{u}_j|}{\gamma}\right) + \hat{\mathbf{z}} \frac{i}{\gamma} K_0\left(\frac{q_z |\mathbf{u}_j|}{\gamma}\right) \right], \end{aligned}$$

where  $K_0$  and  $K_1$  are modified Bessel functions of the second kind and  $\mathbf{u}_j = \mathbf{R} - \mathbf{R}_j$ . In what follows, we present numerical results obtained by evaluating these expressions for either incident electron plane waves (uniform  $\psi_{i\perp}$ ) or Gaussian beams ( $\psi_{i\perp} \propto e^{-R^2/\Delta^2}$ ). We consider transitions to a vortex electron carrying a definite amount of OAM  $\hbar m_f$  [i.e.,  $\psi_{f\perp} \propto e^{im_f\phi} J_{m_f}(P_f R)$ ], characterized by an orbital momentum number  $m_f$  and transversal wave vector  $P_f$  (see the Supplemental Material [24] for further details).

Inspired by the concept of circular dichroism in optics, we define dichroism in electron energy-loss spectroscopy (EELS) as the difference in the loss probability of electron vortices with opposite OAM (e.g.,  $\pm\hbar$ ). We envision an experiment in which the orbital number  $m_f$  can be pre (post)-selected by means of an OAM analyzer placed before (after) the sample. Although the design and fabrication of OAM analyzers still pose a tremendous experimental challenge, excellent progress has been recently made in this direction [5,36–38]. For simplicity, we study incident beams without a net OAM interacting with chiral samples and resolved in OAM components by a post-selection analyzer, although the present work can be trivially extended to deal with pre-selection analyzers. In particular, we first consider a 100 keV plane-wave electron passing through a chiral sample and subsequently entering an OAM analyzer, which deflects different  $m_f$  components along different outgoing directions [see Fig. 1(a)]. Energy loss spectra are recorded for several  $m_f$ 's through an angle-resolved spectrometer. In the Fourier plane, the transmitted  $m_f = \pm 1$  signals display a characteristic annular pattern, in contrast to the more intense  $m_f = 0$  disklike angular map.

We obtain the  $m_f$ -resolved loss cross section  $\sigma_{m_f}(\omega)$  for the incident plane wave by multiplying the transition probability by the wave front area (see the Supplemental Material [24]). The spectrally resolved cross section exhibits complex features with several peaks, corresponding to the excitation of plasmons in the cluster [Fig. 1(b)]. The  $m_f = \pm 1$  spectra show slightly different intensity for each of the spectral features. This prompts us to define the absolute and relative degrees of dichroism associated with the orbital number  $m_f$  as  $\sigma_{m_f} - \sigma_{-m_f}$  and  $(\sigma_{m_f} - \sigma_{-m_f})/(\sigma_{m_f} + \sigma_{-m_f})$ , respectively. For the clusters under consideration, these quantities decrease with increasing  $m_f$  [see Fig. 1(b)].

We study the  $m_f = 1$  dichroism produced by different clusters in Fig. 2. The relative electron dichroism reaches up to  $\sim 10\%$ , which is remarkably high compared with typical values in its optical counterpart [16,17]. As expected, the effect changes sign upon mirror reflection of the sample, while a cluster formed by only three particles lying on a plane normal to the beam does not produce dichroism at all, as it is not seen as chiral by the electron [Figs. 2(a), 2(b)]. In contrast, a net dichroism effect is observed for the trimer by tilting it [Fig. 2(c)], so that the electron sees again a staircaselike structure along the direction of electron propagation. In optics, this

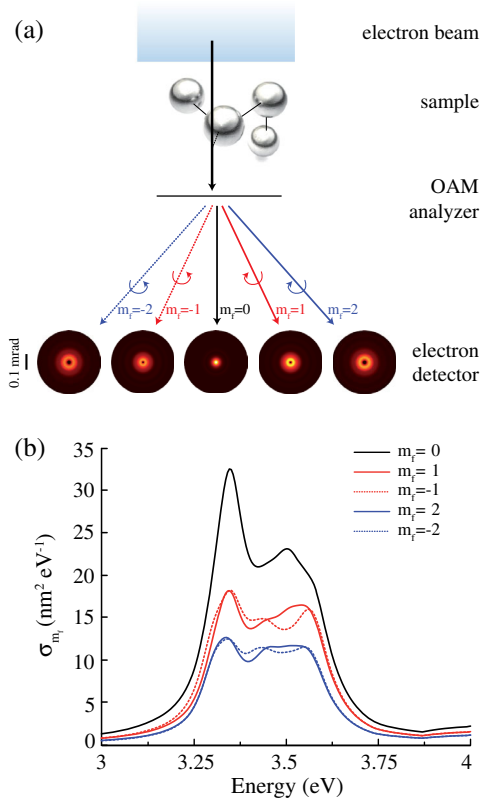


FIG. 1 (color online). (a) Sketch of the system under consideration. A 100 keV electron plane wave impinges on a cluster (left-handed tetramer) consisting of four 30 nm silver spheres separated by 5 nm gaps. The electron is subsequently passing through an orbital angular momentum (OAM) analyzer that splits the beam into different components  $m_f$  along different transmission directions. These components are independently energy-analyzed by an angle-resolved spectrometer. The origin of OAM is made to coincide with the position of the electron arrow depicted in (a). The angular distribution of different  $m_f$  components are represented at the bottom for a 3.5 eV energy loss. For visualization purposes, the intensities of the  $m_f = \pm 1$  and  $m_f = \pm 2$  components are multiplied by factors of 5 and 10, respectively. (b) Energy-loss  $m_f$ -resolved cross-section spectra under the conditions of (a).

phenomenon is known as extrinsic dichroism, which is produced when oriented nonchiral molecules form a chiral triad with the light wave vector [39–41]. This is precisely what happens when the normal of the plane that contains the cluster is tilted with respect to the electron incidence direction, and once more, the effect changes sign upon mirror reflection of the sample. However, this apparent chirality is erased when averaging over all cluster orientations. It is important to stress that the fraction of inelastically scattered electrons that transfer OAM is actually large, as shown in Fig. 2(d) by comparing  $m_f = \pm 1$  and  $m_f = 0$  components.

Particle size and separation in the clusters play an important role in determining the strength of the chiral coupling to the electron (see Fig. S3 in the Supplemental

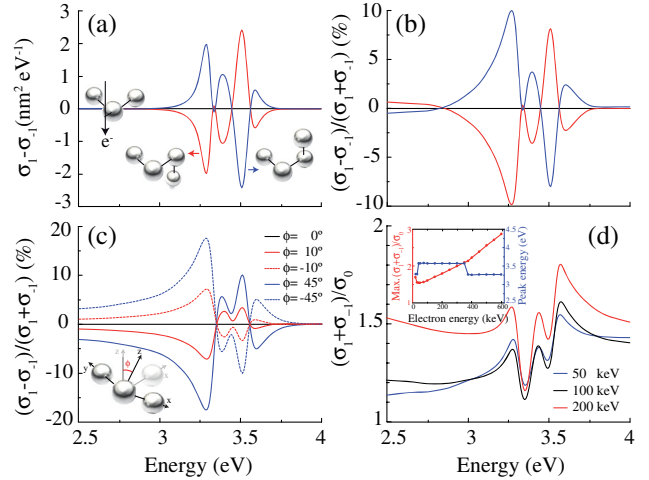


FIG. 2 (color online). (a) Dichroism between  $m_f = \pm 1$  components in the spectrally resolved inelastic cross section of 100 keV electrons for different clusters of 30 nm silver spheres with gaps of 5 nm (see insets). The planar trimer does not exhibit any dichroism. (b) Same as (a), normalized to the sum of  $m_f = \pm 1$  cross sections. (c) Extrinsic dichroism displayed by the trimer when it is tilted with respect to the direction of electron propagation. (d) Partial  $m_f = \pm 1$  inelastic cross sections normalized to the  $m_f = 0$  transmitted beam component for different electron energies in the left-handed tetramer [upper inset in (a)]. The inset of (d) shows the maximum of this ratio (left, red curve) and the energy loss at which this happens (right, blue curve) as a function of electron energy. The origin of OAM is the same as in Fig. 1

Material [24]). Both the EELS intensity and the dichroism increase with particle size, but the latter is reduced with particle separation, as close interaction between the spheres is required to sustain a strong chiral plasmon that extends over the entire cluster.

The coupling to different chiral modes of the sample is also strongly affected by the relative position and alignment between the cluster and the vortex generator (see Fig. S3 in the Supplemental Material [24]). More precisely, the origin of electron OAM (i.e., the origin of azimuthal angles  $\varphi$ ) depends on the design and position of the OAM analyzer. This poses an experimental challenge to measure the dichroic signal. If the planes of the sample and the OAM analyzer are taken to be conjugated in the electron optics setup, with a 1:100 demagnification factor for the analyzer, relative alignment requires sub-micron-scale displacements of the analyzer to produce nanometer-scale displacements at the conjugated sample plane.

Due to conservation of angular momentum, the OAM transferred by the electron produces a mechanical torque on the cluster, which can be separated into two different contributions: intrinsic torque acting on each individual particle and extrinsic torque acting on the cluster as a whole relative to the origin of electron OAM. Additionally, cathodoluminescence emission can take a net amount of angular momentum that needs to be included in this balance. As we show in the Supplemental Material [24],

neglecting retardation, the increase in angular momentum (intrinsic + extrinsic) produced by the self-consistent electromagnetic field resulting from interaction with the electron exactly accounts for the electron momentum transfer (see Fig. S4 in the Supplemental Material [24]).

The excellent spatial resolution of electron microscopes for visualizing optical near fields [23,42,43] can be used to study the chirality associated with each of the plasmon features. Remarkably, we find the relative degree of dichroism to display a sign and magnitude that are rather independent of the lateral width of the electron beam, although the absolute effect quickly vanishes for beams that are much narrower than the size of the plasmon modes (see Fig. S1 of the Supplemental Material [24]).

*Chiral molecule.*—Many biomolecules such as proteins and nucleic acids are chiral. Their optical response can be characterized by nonorthogonal electric (polar vector) and magnetic (axial vector) dipoles that, combined, break mirror symmetry [44]. In particular, the generalized polarizability of a chiral molecule contains electric ( $\alpha_{EE}$ ), magnetic ( $\alpha_{MM}$ ), and magnetoelectric ( $\alpha_{ME} = -\alpha_{EM}^T$ , due to reciprocity [45]) components that are combined in the matrix

$$\boldsymbol{\alpha} = \begin{bmatrix} \alpha_{EE} & \alpha_{EM} \\ \alpha_{ME} & \alpha_{MM} \end{bmatrix}.$$

Dichroism arises from the off-diagonal elements. The electromagnetic matrix element  $\mathbf{N} = [\mathbf{N}_{EE}, \mathbf{N}_{ME}]$  also consists of two different components,

$$\begin{aligned} \mathbf{N}_{EE} &= \int d^2\mathbf{R} \psi_{f\perp}^*(\mathbf{R}) \psi_{i\perp}(\mathbf{R}) \\ &\quad \times \left[ \frac{\mathbf{u}_0}{|\mathbf{u}_0|} K_1 \left( \frac{q_z |\mathbf{u}_0|}{\gamma} \right) + \hat{\mathbf{z}} \frac{i}{\gamma} K_0 \left( \frac{q_z |\mathbf{u}_0|}{\gamma} \right) \right], \\ \mathbf{N}_{ME} &= \frac{v}{c} \int d^2\mathbf{R} \psi_{f\perp}^*(\mathbf{R}) \psi_{i\perp}(\mathbf{R}) K_1 \left( \frac{q_z |\mathbf{u}_0|}{\gamma} \right) \left( \hat{\mathbf{z}} \times \frac{\mathbf{u}_0}{|\mathbf{u}_0|} \right). \end{aligned}$$

Remarkably, the ME crossed term is proportional to the ratio between the electron and light velocities, therefore suggesting that higher-energy electrons are better suited to study chiral molecules.

In Fig. 3 we study  $\sigma_1$  (left panels) and the dichroism  $|\sigma_1 - \sigma_{-1}|$  (right panels) as a function of energy loss for a model point structure (upper panels) and an  $\alpha$ -helix molecule (lower panels). They are both considered to be randomly oriented and placed a distance  $R_0$  apart from the origin of OAM. The model structure has a single chiral resonance of frequency  $\omega_0$ , spectral width  $\gamma_0$ , and associated electric and magnetic dipole moments  $\mathbf{p}$  and  $\mathbf{m}$ , respectively. The maxima of  $\sigma_1$  and  $|\sigma_1 - \sigma_{-1}|$  are normalized to yield the universal curves shown in Figs. 3(a), 3(b), which only depend on electron energy and  $\omega_0 R_0 / v\gamma$ . These results can be applied to molecules and metamolecules [45] by simply plugging their corresponding spectral parameters. It is common to have  $|\mathbf{m}| \ll |\mathbf{p}|$ , so that the cross section is roughly proportional to  $|\mathbf{p}|^2$ , whereas the dichroism scales as  $|\mathbf{m} \cdot \mathbf{p}|$ . Interestingly,

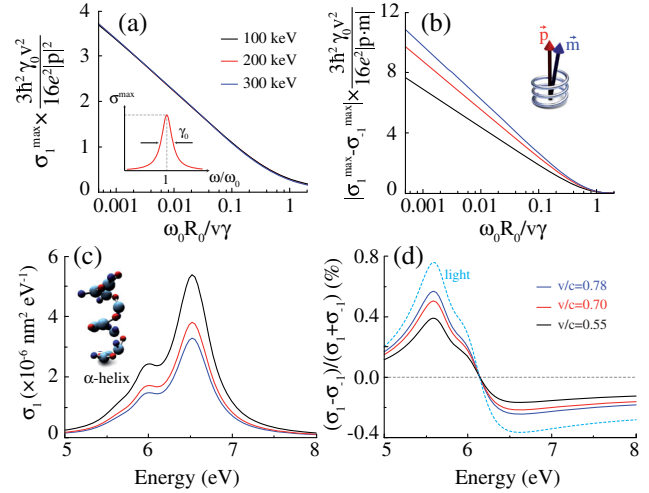


FIG. 3 (color online). (a),(b) Normalized maximum of the partial inelastic cross section  $\sigma_1$  (a) and the dichroism  $|\sigma_1 - \sigma_{-1}|$  (b) for a randomly oriented model point structure characterized by a chiral excitation of frequency  $\omega_0$ , width  $\gamma_0$ , and associated electric and magnetic dipole moments  $\mathbf{p}$  and  $\mathbf{m}$  [see inset to (b)]. The cross section and dichroism spectra follow a Lorentzian profile [see inset to (a)]. The origin of OAM is displaced a distance  $R_0$  with respect to the structure. The vertical axes are normalized to yield universal curves that only depend on the electron energy (see legend) and  $\omega_0 R_0 / v\gamma$ . (c),(d) Partial inelastic cross section (c) and normalized dichroism (d) for an  $\alpha$ -helix, parametrized as described in the Supplemental Material [24]. The optical dichroism with circularly polarized light is shown for reference. Different electron energies are considered with the same color code throughout the figure.

the absolute dichroism diverges logarithmically with decreasing  $R_0$ , thus suggesting a possible approach towards ultra-sensitive detection of chirality consisting in lowering  $R_0$  by employing a highly demagnified OAM analyzer.

Results for the  $\alpha$ -helix biomolecule—a common secondary structure of proteins—are presented in Figs. 3(c), 3(d) using fitted parameters to model its three main UV resonances (see the Supplemental Material [24]) and taking  $R_0 = 1$  nm. The universal curves obtained for the model structure provide a reasonable description of the spectra associated with each of these resonances. Interestingly, the calculated dichroism has a similar magnitude and profile as the optical dichroism that is obtained by replacing  $\sigma_{\pm 1}$  by the extinction cross section of right (+1) and left (−1) circularly polarized light [Fig. 3(d)]. In practice, electron dichroism could be measured in molecular ensembles, which we predict to produce loss intensities comparable with those measured for nanoparticle plasmons [23] when the electrons are passing  $\sim 1$  nm apart from a few tens of molecules.

*Concluding remarks.*—We predict large transfers of orbital angular momentum and a remarkably high degree of dichroism in the inelastic interaction of electron beams with chiral structures. Unlike light, electrons can engage in dichroic transfer of orbital angular momentum, which provides an extra tool for probing intrinsic and extrinsic

rotational degrees of freedom. Combined with the spatial resolution of electron microscopes, this can be used to map different chiral modes in plasmonic structures, which are important elements of chiral metamaterials. The dichroism signal changes sign when mirror imaging the sample, and it disappears in systems that have mirror symmetry with respect to a plane perpendicular to the beam direction. The strength of the absolute dichroism is strongly dependent on the degree of focusing of the electron beam, and it is maximized when the beam size is comparable to the extension of the probed chiral mode. We also demonstrate that electron vortex beams can resolve the handedness of chiral biomolecules, which has great potential for biological and pharmaceutical studies.

We thank Johan Verbeeck and Giulio Guzzinati for helpful discussions and for a critical revision of the Letter. A. A.-G. acknowledges support through FPU from MEC.

\*javier.garciadeabajo@icfo.es

- [1] K. Y. Bliokh, Y. P. Bliokh, S. Savel'ev, and F. Nori, *Phys. Rev. Lett.* **99**, 190404 (2007).
- [2] M. Uchida and A. Tonomura, *Nature (London)* **464**, 737 (2010).
- [3] J. Verbeeck, H. Tian, and P. Schattschneider, *Nature (London)* **467**, 301 (2010).
- [4] B. J. McMorran, A. Agrawal, I. M. Anderson, A. A. Herzing, H. J. Lezec, J. J. McClelland, and J. Unguris, *Science* **331**, 192 (2011).
- [5] K. Saitoh, Y. Hasegawa, K. Hirakawa, N. Tanaka, and M. Uchida, *Phys. Rev. Lett.* **111**, 074801 (2013).
- [6] T. T. Wu and C. N. Yang, *Nucl. Phys.* **B107**, 365 (1976).
- [7] A. Béché, R. Van Boxem, G. Van Tendeloo, and J. Verbeeck, *Nat. Phys.* **10**, 26 (2014).
- [8] S. M. Lloyd, M. Babiker, and J. Yuan, *Phys. Rev. Lett.* **108**, 074802 (2012).
- [9] P. Schattschneider, S. Löffler, M. Stöger-Pollach, and J. Verbeeck, *Ultramicroscopy* **136**, 81 (2014).
- [10] J. Rusz and S. Bhowmick, *Phys. Rev. Lett.* **111**, 105504 (2013).
- [11] Z. Mohammadi, C. P. Van Vlack, S. Hughes, J. Bornemann, and R. Gordon, *Opt. Express* **20**, 15024 (2012).
- [12] C. Greenshields, R. L. Stamps, and S. Franke-Arnold, *New J. Phys.* **14**, 103040 (2012).
- [13] K. Y. Bliokh, P. Schattschneider, J. Verbeeck, and F. Nori, *Phys. Rev. X* **2**, 041011 (2012).
- [14] J. Verbeeck, H. Tian, and G. V. Tendeloo, *Adv. Mater.* **25**, 1114 (2013).
- [15] S. M. Lloyd, M. Babiker, and J. Yuan, *Phys. Rev. A* **88**, 031802 (2013).
- [16] *Molecular Light Scattering and Optical Activity*, edited by L. D. Barron (Wiley, New York, 2004).
- [17] D. B. Amabilino, *Chirality at the Nanoscale* (Wiley, New York, 2009).
- [18] D. L. Andrews, L. C. Dávila Romero, and M. Babiker, *Opt. Commun.* **237**, 133 (2004).
- [19] M. M. Coles and D. L. Andrews, *Phys. Rev. A* **85**, 063810 (2012).
- [20] S. M. Lloyd, M. Babiker, and J. Yuan, *Phys. Rev. A* **86**, 023816 (2012).
- [21] F. Araoka, T. Verbiest, K. Clays, and A. Persoons, *Phys. Rev. A* **71**, 055401 (2005).
- [22] W. Löffler, D. J. Broer, and J. P. Woerdman, *Phys. Rev. A* **83**, 065801 (2011).
- [23] F. J. García de Abajo, *Rev. Mod. Phys.* **82**, 209 (2010).
- [24] See the Supplemental Material, which includes Refs. [25–28], at <http://link.aps.org/supplemental/10.1103/PhysRevLett.113.066102>, where we provide detailed derivations of all equations and formalism used in this paper, including expressions for the inelastic electron transition probability, the polarizability of spherical particles and chiral molecules, the Green tensor of a sphere cluster, and a parametrization of the absorption bands of the  $\alpha$ -helix. We also include studies of the dependence of electron dichroism on relevant beam and sample parameters, the effect of sphere multipoles, and the conservation of linear and angular momentum during electron-sample interaction.
- [25] F. J. García de Abajo, *Phys. Rev. B* **60**, 6086 (1999).
- [26] B. T. Draine and P. J. Flatau, *J. Opt. Soc. Am. A* **11**, 1491 (1994).
- [27] A. O. Govorov, Z. F. P. Hernandez, J. M. Slocik, and R. R. Naik, *Nano Lett.* **10**, 1374 (2010).
- [28] W. C. Johnson and I. Tinoco, *J. Am. Chem. Soc.* **94**, 4389 (1972).
- [29] H. Raether, *Surface Plasmons on Smooth and Rough Surfaces and on Gratings*, Springer Tracks in Modern Physics Vol. 11 (Springer-Verlag, Berlin, 1988).
- [30] C. J. Powell and J. B. Swan, *Phys. Rev.* **115**, 869 (1959).
- [31] J. K. Gansel, M. Thiel, M. S. Rill, M. Decker, K. Bade, V. Saile, G. von Freymann, S. Linden, and M. Wegener, *Science* **325**, 1513 (2009).
- [32] A. Kuzyk, R. Schreiber, Z. Fan, G. Pardatscher, E.-M. Roller, A. Högele, F. C. Simmel, A. O. Govorov, and T. Liedl, *Nature (London)* **483**, 311 (2012).
- [33] X. Shen, A. Asenjo-Garcia, Q. Liu, Q. Jiang, F. J. García de Abajo, N. Liu, and B. Ding, *Nano Lett.* **13**, 2128 (2013).
- [34] J. Zuloaga, E. Prodan, and P. Nordlander, *Nano Lett.* **9**, 887 (2009).
- [35] P. B. Johnson and R. W. Christy, *Phys. Rev. B* **6**, 4370 (1972).
- [36] T. S. Yahn, J. S. Pierce, T. R. Harvey, and B. J. McMorran, *Microsc. Microanal.* **19**, Suppl. 2, 1166 (2013).
- [37] G. Guzzinati, L. Clark, A. Béché, and J. Verbeeck, *Phys. Rev. A* **89**, 025803 (2014).
- [38] L. Clark, A. Béché, G. Guzzinati, and J. Verbeeck, *Phys. Rev. A* **89**, 053818 (2014).
- [39] C. W. Bunn, *Chemical Crystallography* (Oxford University, New York, 1945).
- [40] R. Williams, *Phys. Rev. Lett.* **21**, 342 (1968).
- [41] E. Plum, X.-X. Liu, V. A. Fedotov, Y. Chen, D. P. Tsai, and N. I. Zheludev, *Phys. Rev. Lett.* **102**, 113902 (2009).
- [42] J. Nelayah, M. Kociak, O. Stéphan, F. J. García de Abajo, M. Tencé, L. Henrard, D. Taverna, I. Pastoriza-Santos, L. M. Liz-Marzán, and C. Colliex, *Nat. Phys.* **3**, 348 (2007).
- [43] D. Rossouw, M. Couillard, J. Vickery, E. Kumacheva, and G. A. Botton, *Nano Lett.* **11**, 1499 (2011).
- [44] N. Berova, K. Nakanishi, and R. W. Woody, *Circular Dichroism: Principles and Applications* (VCH, New York, 1994).
- [45] I. Sersic, C. Tuambilangana, T. Kampfrath, and A. F. Koenderink, *Phys. Rev. B* **83**, 245102 (2011).